# Microphysical characteristics of precipitation within convective overshooting over East China observed by GPM DPR and ERA5

Nan Sun[1], Gaopeng Lu[1], Yunfei Fu[1]

[1]School of Earth and Space Sciences, University of Science and Technology of China, Hefei, 230026, China

*Corresponding to*: Yunfei Fu, fyf@ustc.edu.cn

**Abstract.** We examine the geographical distribution and microphysical three-dimensional structure of convective overshooting over East China by matching Global Precipitation Measurement Dual-frequency Precipitation Radar instrument (GPM DPR) with European Centre for Medium-Range Weather Forecasts 5th Reanalysis (ERA5). Convective overshooting mainly occur over Northeast China (NC) and northern Middle and East China (MEC) and its frequency varies from $4\times10^{-4}$ to $5.4\times10^{-3}$. Radar reflectivity of convective overshooting over NC accounts for a higher proportion below the freezing level, while MEC and South China (SC) account for a higher proportion above the freezing level, indicating stronger upward motion and more ice crystal particles. The microphysical processes within convective overshooting are unique, leading to various properties of the droplets in precipitation. Droplets of convective overshooting are large, but sparse, with an effective droplet radius of nearly 2.5 mm below 10 km, which is about twice that of non-overshooting precipitation. Findings of this study may have important implications for the microphysical evolution associated with convective overshooting, and provide more accurate precipitation microphysical parameters as input for model simulations.

## 1 Introduction

Convective overshooting provides a rapid transport mechanism that can irreversibly transport water vapor and chemical constituents from lower troposphere to the upper troposphere and lower stratosphere (UTLS) by mixing them with environmental air (Fueglistaler et al., 2004; Frey et al., 2015), which has a direct impact on radiation balance and global climate change (Solomon et al., 2010). As one of the main sources of ozone destroying OH hydroxyl radicals, stratospheric water vapor can help to destroy ozone, which has potential effects on radiative forcing (Anderson et al., 2012). Water vapor enters the stratosphere mainly through the tropical tropopause layer. Several studies show that tropical convective overshooting has a net dehydrating effect on the stratospheric humidity (Danielsen, 1993; Sherwood and Dessler, 2001), while modeling and observational studies have universally show tropical convective overshooting hydrating the stratosphere (Chaboureau et al. 2007; Jensen et al. 2007; de Reus et al. 2009; Avery et al. 2017) because of the injection of ice mass into the stratosphere (Grosvenor et al., 2007; Corti et al., 2008; Chemel et al., 2009; Khaykin et al., 2009). In midlatitude, observations and model simulations show that deep convective overshooting is also an important source for the lower stratospheric water vapor (Liu and Liu, 2016; Smith et al., 2017; Liu et al., 2020; Werner et al., 2020; Wang et al., 2023). Wang et al. (2023) use a high-resolution numerical model to study convective overshooting moistening in the midlatitude lower stratosphere and results show that convective water vapor plumes above 380-K temperature are stable in the stratosphere, while that closer to the tropopause and cloud tops are less stable. In addition to these impacts on water vapor, the effects of convective overshooting on the temperature of the UTLS have also attracted much attention (Sherwood et al., 2003; Chae et al., 2011; Biondi et al., 2012).In addition to UTLS composition effects, convective overshooting is often associated with severe and hazardous weather (e.g., heavy rain, hail, tornadoes, and strong winds) at the Earth's surface, with important social and economic impacts (Line et al., 2016; Bedka et al., 2018; Marion et al., 2019). Given these potentially significant impacts, it is of high importance to understand the characteristics of convective overshooting, which have attracted considerable attention in recent years (Johnston et al., 2018; Muhsin et al., 2018).

Perhaps one of the most poorly understood features of convective overshooting is the microphysical structure of precipitation, such as particle size, concentration, phase state and other parameters. Understanding the microphysical characteristics of convective overshooting is helpful to clarify the efficiency of water vapor transport to the lower stratosphere by convective overshooting. In addition, the microphysical processes within convective overshooting are closely related to storm dynamics and thermodynamics through latent heat, and the quantitative description of microphysical characteristics is helpful to improve the accuracy of model simulation parameters (Homeyer and Kumjian, 2015). Liu et al. (2012) studied the climatological characteristics of convective overshooting and found convective overshooting show remarkable regionality and seasonal variations.. Homeyer and Kumjian (2015) observed the radar reflectivity characteristics of convective overshooting from the analysis of the polarimetric radar observations. Although the above studies have explored the characteristics of some precipitation parameters within convective overshooting, we still lack the understanding of more precipitation microphysical parameters and more detailed microphysical processes within convective overshooting due to the limitations of observation methods.

To fully study the microphysical characteristics of convective overshooting, accurate methods of detecting the frequency and long-term distribution of convective overshooting are required. The traditional way for detecting convective overshooting from satellite is to find pixels in infrared imagery with brightness temperatures colder than a given temperature threshold (Machado et al. 1998; Rossow and Pearl 2007). Gettelman et al. (2002) have studied the cloud regions colder than the tropopause temperature on infrared images and found that the frequency of tropical convective overshooting is about 0.5%. However, it is impossible to guarantee that the low value of infrared brightness temperature represents clouds penetrating the tropopause rather than cirrus or cloud anvil in the upper air due to the lack of vertical structure information of convection. Also, overshoots mix with relatively warm stratosphere air such that cold pixels are often diminish and not a reliable means to identify overshooting. With the launch of Precipitation Radar aboard Tropical Rainfall Measuring Mission (TRMM), three-dimensional structure information of precipitation within the convective overshooting can be provided (Alcala and Dessler, 2002; Liu and Zipser, 2005) and a new method for detecting the convective overshooting is proposed that is to find pixels with rain top height higher than tropopause height (Xian and Fu, 2015; Sun et al., 2021), which improves the accuracy of detecting convective overshooting. Still, TRMM PR can't provide the precipitation microphysical information, which limits our study on the internal microphysical structure within convective overshooting. Besides, TRMM PR can underestimate the height of convective overshooting because of only sensitive to large precipitation particles (sensitivity at ~17 dBZ) (Hanii and Zheng, 2014).

As the continuation of TRMM PR, Global Precipitation Measurement (GPM) carrying the first Dual-frequency Precipitation Radar (DPR) launched in February 2014. GPM DPR include two bands of precipitation radar, which provides excellent opportunities for studying the microphysical structure of precipitation (Sun et al., 2022a). Liu et al. (2016, 2020) have used GPM KuPR and ERA-Interim 6-hourly datasetto study climatology and detection of convective overshooting. However, the above studies only use the KuPR data and mainly focus on the geographical distribution; the microphysical processes of convective overshooting remain unknown.

Another difficulty in convective overshooting detection is to obtain tropopause height data with high spatial and temporal resolution. On the one hand, the determination of the tropopause is still under debate. At present, the following four definitions of the tropopause are widely adopted throughout the world: Cold point tropopause, thermal tropopause, dynamic tropopause and ozone tropopause. Cold point tropopause is only physically meaningful in the latitude zone 10 °S-10 °N near the equator (Highwood and Hoskins, 1998; Rodriguez-Franco and Cuevas, 2013). Dynamic tropopause is based on the differing values of potential vorticity in the troposphere and stratosphere, which applies to extratropical areas (Danielsen et al., 1987; Holton et al., 1995). Ozone tropopause is defined based on the ozone sounding profiles, whose disadvantage is that the choice of ozone mixing ratio thresholds varies with region and season (Bethan et al., 1996; Zahn et al., 2004). Therefore, this paper uses the thermal tropopause, which is defined by the World Meteorological Organization (WMO) (WMO, 1957). The thermal tropopause is based on the temperature lapse rate, also known as lapse-rate tropopause. The accurate calculation of the tropopause height based on this definition, on the other hand, depends on the temperature profile data with high spatial and temporal resolution. The latest generation of reanalysis data ERA5 provides hourly estimates of a large number of atmospheric, land and oceanic climate variables, which has attracted much attention due to its much higher spatial and temporal resolution than its predecessor ERA-Interim, especially in the upper troposphere and lower stratosphere (Hoffmann et al. 2019). Sun et al. (2022b) verified the accuracy for the tropopause height calculated from temperature profiles of ERA5 by comparing ERA5 with other popular datasets.

East China is located in the East Asian monsoon region, with unique climate characteristics. The precipitation of East China in summer is affected by the circulation anomalies of the East Asian tropical and subtropical monsoon and their interactions. The precipitation anomalies not only have an important impact on industrial and agricultural production, social infrastructure construction, but also threaten the safety of human life and property. Many scholars have studied the characteristics of precipitation in East China (Zhang et al., 2018; Xu, 2020), but few have studied the characteristics of convective overshooting and its internal precipitation microphysical structure over East China. The purpose of this study is to examine the microphysical characteristics of convective overshooting over East China by matching the precipitation data from GPM DPR and meteorological parameters from ERA5.

## 2 Data and method

### 2.1 DPR-based precipitation dataset

GPM DPR include KuPR (Ku band, 13.6 GHz) and KaPR (Ka band, 35.5 GHz), two bands of precipitation radar. KuPR is similar to TRMM PR and has a longer wavelength, which is better at detecting heavy precipitation (the minimum detected precipitation is about 0.5 mm/h). However, KaPR has a shorter wavelength, which is more sensitive to weak precipitation (the minimum detected precipitation is about 0.2 mm/h). Based on the different echo characteristics of Ku band and Ka band, the dual channel inversion algorithm can be used to retrieve Droplet Size Distribution (DSD). Here we use the precipitation datasets are provided by the GPM level 2 product 2ADPR in version 6. The horizontal resolution is 5 km and the vertical resolution is 125m. The precipitation microphysical parameters provided by GPM 2ADPR include droplet concentration ($dBN_0$) and effective radius ($D_0$).

### 2.2 ERA5-based meteorological dataset

The meteorological data are from ERA5 reanalysis product, whose name is "ERA5 hourly data on pressure levels from 1940 to present". . And the following parameters are used in this paper: temperature, specific humidity, vertical velocity, ozone mass mixing ratio, U-component of wind, and V-component of wind. The time resolution is 1 h and the horizontal resolution is 0.25 ° × 0.25 °. Vertical coverage is 1000 hPa to 1hPa and vertical resolution is 37 pressure levels (1000, 975, 950, 925, 900, 875, 850, 825, 800, 775, 750, 700, 650, 600, 550, 500, 450, 400, 350, 300, 250, 225, 200, 175, 150, 125, 100, 70, 50, 30, 20, 10, 7, 5, 3, 2, 1 hPa).

### 2.3 Detection method of convective overshooting

Firstly, match each pixel of GPM DPR detection with ERA5 grid data by using the principle of the nearest method. The marching time between GPM and ERA5 is 1 h, and the matching range is 0.25 ° ×

0.25°. Storm top height is obtained from the GPM DPR. Convective overshooting is defined to occur where the storm top height is above the real-time tropopause height in a precipitation pixel.

Real-time tropopause height is calculated from the temperature profiles from ERA5 according to the definition from the World Meteorological Organization (WMO, 1957). The algorithmic process is shown as follows: Firstly, find X layer whose atmospheric lapse rate is 2 K $km^{-1}$ or less starting from the first layer (near the ground) of the temperature profile, and then judge whether the atmospheric lapse rate does not exceed 2 K $km^{-1}$ between the X level and all higher levels within 2 km, if so, the height of X layer is the tropopause height, if not, repeat the above algorithm starting from the X layer until tropopause layer is found.

**2.4 Study areas**

The study areas are marked as black boxes in Fig. 1a and only the land parts are studied because characteristics of vertical structure of precipitation over land and sea are very different, and this study is limited in space and focuses only on the land region. Using years of NCEP/NCAR reanalysis data, Xia (2015) analyzed the climatic feature of temperature and water vapor in China and divided China into different climatic zones. To have a better understanding of precipitation microphysical structure over different regions of East China, we also divided East China into three climatic zones according to its climatic characteristics and previous studies (Xia, 2015; Sun et al., 2022a). From north to south, they are Northeast China (NC, 38°–50°N, 118°–130°E), Middle and East China (MEC, 26.5°–38°N, 112°–123°E), and South China (SC, 18°–26.5°N, 108°–123°E). For the three regions, the lower latitude areas have higher surface temperature, greater temperature lapse rate and lower temperature of stratosphere. Temperature profiles of same latitude are essentially same over SC and MEC, and temperature signals exist meridional differences over NC. Atmospheric humidity has remarkable regional characteristics. SC is wetter, with the surface relative humidity of more than 70%, while NC and MEC are drier and their humidity range from 50% to 70% (Xia, 2015). The study time frame is defined as the time from 2014 to 2020 in summer (June, July and August)

## 3 Results

### 3.1 Case studies

Three cases selected from NC, MEC and SC are analyzed to lay a foundation for the subsequent statistical analysis. The precipitation characteristics of the three cases are shown as Fig. 2. The Case 1 (C1) occurs in NC at 14:00 on July 1, 2017. Convective overshooting is observed in a total of 65 pixels for C1, whose mean rain rate are 20.7 mm/h (Fig. 2a) and mean storm top height are 14.1 km (Fig. 2b). The strong radar reflectivity along A1B1 occurs at 35-95km away from point A1, and the strongest echo is up to 50 dBZ, appears at 0-5 km (Fig. 2c). The maximum echo height is about 15 km, 2 km higher than the tropopause height. The Case 2 (C2) occurs in MEC at 13:00 on July 30, 2015. Convective overshooting is observed in a total of 58 pixels for C2, and their mean rain rate are 29.7 mm/h (Fig. 2d) and mean storm top height are 15.2 km (Fig. 2e). The radar echo along A2B2 is very strong and the strongest echo is up to 50 dBZ, which is about 45-95 km away from point A2 (Fig. 2f). The highest echo can reach to about 17 km altitude. The Case 3 (C3) occurs in SC at 17:00 on June 13, 2015. Convective overshooting is observed in a total of 8 pixels for C3 and their mean rain rate are 46.3 mm/h (Fig. 2g) and mean storm top height are 16.9 km (Fig. 2h). The strongest echo occurs at 60-70 km away from point A3 and the highest echo can reach to 17.2 km, about 0.5 km higher than the tropopause height (Fig. 2i).

To learn about the characteristics of the large scale circulation for these three cases, we calculate the distribution of Precipitable Water Vapor (PWV), streamlines and Vertical Velocity (VV), and locations of the three cases are shown as the black boxes in Fig. 3. In general, areas in which convective overshooting occur have abundant PWV and strong ascending movement. In C1, The PWV of the region in which convective overshooting occurs is between 50 and 55 mm, which is higher than otherwise (Fig. 3a). Upward motionnear the convective overshooting is strong, ranging from -0.03 to -0.12 Pa/s, contributing to the occurrence of convective overshooting (Fig. 3b). The PWV of C2 is more abundant than C1, and the PWV of the area in which convective overshooting occurs are between 55 and 60 mm (Fig. 3c). The VV near the convective overshooting is mostly between -0.09 and -0.15 Pa/s (Fig. 3d). In C3, the PWV near the precipitation area and convective overshooting area are the most abundant compared with C1 and C2, whose maximum can exceed 70 mm (Fig. 3e). Upward movement near the precipitation area and convective overshooting area are very strong and the VV are between -0.12 and

-0.18 Pa/s, which provide abundant water vapor and dynamic conditions for the occurrence of convective overshooting.

### 3.2 Statistical results

#### 3.2.1 Geographical distribution

Firstly, the horizontal distribution characteristics of convective overshooting over East China are analysed by designing a more accurate algorithm for convective overshooting determination. Accurate determination of tropopause height is the first step of the convective overshooting determination algorithm. We first analyze geographical distribution of climatological mean of the tropopause height over East China calculated from ERA5, shown as Fig. 1b. In general, the tropopause height over East China is between 11.6 km and 16.7 km and has an obvious zonal distribution pattern: Tropopause height over SC and southern MEC (18-36 °N) is the highest and has small spatial variabilities, concentrated at ~16.7 km. Over northern MEC (36-38 °N), tropopause height decreases and forms a gradient, which decreases to 16 km. Tropopause height over NC is the lowest and continues to decrease in a gradient pattern from south to north, decreasing to 13 km near central NC (45 °N) and 12 km near northern NC (48 °N). Minimum standard deviation of tropopause height appears in SC, along with central and southern MEC, lower than 0.2 km. From northern MEC to northern NC, the standard deviation first increases and then decreases, reaching a maximum of more than 2 km around 42 °N, and standard deviation over NC is generally above 1 km.

Obtaining storm top height from precipitation data is the second step of convective overshooting algorithm. Fig. 4 show geographical distribution of storm top height for total precipitation, convective precipitation and convective overshooting. Total precipitation represent the all pixels with rain rate higher than 0 mm/h detected by GPM DPR, and those pixels whose rain type are “Convective” are defined as convective precipitation. As shown, mean storm top height over East China varies from 4.5 km to 8.5 km, while convective storm top height is mainly distributed between 3.5 km and 9 km. Convective storm top height over NC and northern MEC are the highest, with most areas exceeding 6.5 km and as we noted above, tropopause height in these two regions are lower (Fig. 1b), it can be inferred that convective overshooting events are more likely to occur. Further analysis of the frequency of convective overshooting in the following text will confirm this point. Compared with NC, convective storm top height over SC and southern MEC is lower, mainly distributed below 6.5 km. Storm top height of convective overshooting ranges from 10 km to 21 km (Fig. 4c), much higher than normal precipitation (total and convective precipitation) and increasing gradually from north to south. Storm top heights of convective overshooting over NC and northern MEC are low, distributed between 10 km and 16 km, which is due to a lower tropopause height (Fig. 1b) allowing convection with lower storm top height to reach the stratosphere. This lowers the mean storm top height of convective overshooting in these regions, while tropopause heights over SC and southern MEC range from 16 km to 21 km (Fig. 1b), allowing only strong convection to reach the stratosphere.

The frequency of convective overshooting is defined as the number of convective overshooting events divided by the total observed sample number of GPM DPR. Statistical results indicate that the frequency of the convective overshooting over East China is very low, with a magnitude of only $10^{-3}$, varying regionally (Fig. 5). Sample size of convective overshooting over NC is the highest, followed by MEC, and SC is the lowest (Table 1). Convective overshooting over NC and northern MEC, whose frequency range from $4\times10^{-4}$ to $5.4\times10^{-3}$ (Fig. 5), occur more frequently than SC and southern MEC, whose frequency is between $2\times10^{-4}$ and $6\times10^{-4}$, which is mainly because the former has a lower tropopause height and it's easier for convective overshooting to occur.

### 3.2.2 Vertical structures

Based on the reflectivity profiles and the rain-rate profiles provided by the GPM DPR instrument, we studied the vertical structure of precipitation within convective overshooting. Contoured Frequency by Altitude Diagrams (CFADs) analysis of radar reflectivity can effectively indicate the three-dimensional structure characteristics of precipitation, which is therefore applied in a large number of precipitation studies (Yuter and Houze, 1995). Fig. 6 shows CFADs of the DPR radar reflectivity. In general, radar reflectivity within convective overshooting is stronger and its storm top height is higher. And the CFADs analysis also shows regional differences. Radar echo intensity of convective overshooting over NC is the weakest, and the echo near surface is mainly distributed from 25 dBZ to 55 dBZ, with sharp peak near 47 dBZ, while the peak of the total precipitation is around 16 dBZ. And the max radar echo top within convective overshooting over NC can reach to 13.5 km, 3.3 km higher than the mean precipitation. Compared with NC, radar reflectivity within convective overshooting over SC and MEC are stronger and their CFADs character is more similar. Their echo top height is ~18 km, 6.5 km higher than total precipitation, 4.5 km higher than NC, and their echo near surface concentrated around 30-55 dBZ, while that of total precipitation is between 15 dBZ and 43 dBZ. Besides, Radar reflectivity of convective overshooting over NC accounts for a higher proportion below the freezing level (Altitude where the temperature is 0 ℃), while MEC and SC account for a higher proportion above the freezing level, which indicate that the upward motion within convective overshooting over MEC and SC are stronger and there are larger.

Quantitative analysis of the vertical structure of precipitation within convective overshooting is one of the main issues of interest to this study. Shown as Fig. 7, the rain rate profiles of convective overshooting are provided, and to highlight its unique feature, rain rate profiles of total precipitation and convective precipitation are also given. In general, the rain rate of convective overshooting is much higher, especially below the freezing level (~5 km), 5-10 times that of normal precipitation. This indicates stronger convection and a greater concentration of ice. In addition, differences between three regions are obvious. Rain rate of convective overshooting over NC are about half as high as over MEC and SC, which is consistent with the results of radar echo. At 1 km altitude, rain rate of convective overshooting are 12 mm/h (NC), 22.5 mm/h (MEC), and 23 mm/h (SC) respectively. Below freezing level, the variation of rain rate with altitude is not very obvious, and difference of rain rate between convective overshooting and normal precipitation are ~8 mm over NC and ~20 mm over MEC and SC. Above freezing level, rain rate of convective overshooting clearly decreases with increasing altitude, and rain rates are 6mm/h (NC), 10 mm (MEC) and 6.5mm (SC) at 10 km. However, rain rates of other precipitation are no more than 2 mm/h above 8 km, we therefore suggest that the strong upward flow within convective overshooting brings large amounts of moisture from the lower layer to the upper layer.

We conduct the Probability Density Function (PDF) analysis on the Near Surface Rain Rate (NSRR) within convective overshooting, and that of total and convective precipitation are also calculated, shown as Fig. 8. Grade of precipitation are as follows: Light rain: <4.9 mm/12 h, Moderate rain: 5.0-14.9 mm/12h, Heavy rain: 15.0-29.9 mm/12h, Torrential rain: 30.0-69.9 mm/12h, Downpour: 70.0-139.9 mm/12h, and Heavy downpour: ≥140.0 mm/12h (General Administration of Quality Supervision, 2012). The PDF curve of NSRR of convective overshooting is clearly different from normal precipitation, and has regional differences. The peak value of PDF of convective overshooting appears at ~10 mm/h, classified as downpour, while that of normal precipitation appears at ~1 mm/h, classified as moderate rain, which is obviously lower than convective overshooting. And the PDF of peak value of convective overshooting over NC is about 11.5%, while that over MEC and SC are about 6%. Besides, sample size of convective overshooting with precipitation grade of heavy downpour account for 34.0% (NC)，46.7% (MEC) and 34.8% (SC) respectively, 3-10 times than normal precipitation, which remind us to pay special attention to the extreme precipitation events caused by convective overshooting that may cause harm to our production and life.

### 3.2.3 Microphysical features

GPM center provides particle spectrum from dual-frequency radar. Based on the DSD profiles from 2ADPR, we further investigate the microphysical structures of convective overshooting. The Liquid Water Path (LWP) and Ice Water Path (IWP) show the overall water content in the atmospheric column, which is closely associated with microphysical processes within convective overshooting. To quantify the characteristics of LWP and IWP within convective overshooting, the PDF of LWP and IWP of convective overshooting are shown as Fig. 9, and that of convective and total precipitation are also shown for comparison. The LWP and IWP within convective overshooting are the highest, with high value of PDF mainly distributed around 1000 $g/m^3$ and 5000 $g/m^3$ respectively, much higher than that of normal precipitation, which are around 100 $g/m^3$ and 300 $g/m^3$, indicating sufficient water vapor inside convective overshooting. And differences of IWP between convective overshooting and normal precipitation are bigger than LWP, suggesting that differences of water vapor above freezing level between them is greater and convective overshooting brings water vapor from bottom of the troposphere to higher layers. Besides, differences of LWP and IWP between three regions are also worth noting: The LWP and IWP over MEC and SC are more similar and higher than NC. Especially, LWP over MEC has a bimodal structure with peaks of 630 and 5000 $g/m^3$, which are consistent with the bimodal structure of NSRR PDF curve in Fig. 8. Analysis above in Fig. 1b shows that tropopause height over northern MEC is lower than southern MEC, making it easier for convective overshooting to occur over northern MEC. This indicates that there are two types of convective overshooting events over MEC, weak events with lower storm top height and strong events with higher storm top height, which correspond to the two peaks of LWP PDF curve respectively.

We further use DSD parameter profiles, including the effective radius ($D_0$) and droplet concentration ($dBN_0$) profiles, to analyze the microphysical characteristics within convective overshooting, shown as Fig. 10. Results show that the microphysical processes within convective overshooting are unique, leading to various properties of the droplets in precipitation. Droplets of convective overshooting are large, but sparse. Influenced by strong updrafts, precipitation particles within convective overshooting continuously collide and grow large enough to fall, therefore, the effective radius of droplets are big, below 10 km altitude, almost exceeding 2.5 mm, which is about twice than that of normal precipitation. However, the droplet concentration within convective overshooting is relatively lower. Differences of microphysical structure between three regions are also worth noting. Convective overshooting events over NC have large, but sparse droplets, while that over SC have small, but dense droplets, and the effective radius and concentration of droplets over MEC are between NC and SC, which is speculated that it's related to the differences of aerosol content and types over three regions. Specifically, at 1 km altitude, the effective radius of droplets over NC is the largest (2.87 mm), followed by MEC (2.7 mm), and SC is the lowest (2.5 mm). As altitude increases, the effective radius of droplets first increase and then decrease, with maximum of 2.93 mm over NC at 2.5 km and sharp peak over MEC (2.85 mm) and SC (2.76 mm) near freezing level, about twice than normal precipitation. The effective radius of droplets for convective overshooting over NC and MEC are lower than 2.5 mm above 10 km and 12 km respectively. It's worth noting that the effective radius of droplets for convective overshooting over SC show an increasing trend above 8 km altitude, which are similar to convective precipitation, and their effective radius of droplets over three regions also show an increasing tend from 9 km to 13 km, which may be related to the strong upward motion inside. When the upward motion is strong, ice particles must grow large enough to fall (Langmuir, 1948). Droplet concentration basically decreases with altitude, and that within convective overshooting is obviously lower than normal precipitation and NC is the lowest, while MEC and SC are higher and similar. Droplet concentration within convective overshooting near ground is the highest, with NC (25.4), MEC (28) and SC (28), while that of normal precipitation is mainly distributed between 32 and 35.

## 4 Summary and conclusions

The microphysical characteristics of convective overshooting are essential but poorly understood due to the difficulty in accurately detecting the convective overshooting and obtaining microphysical parameters during severe weather events. Based on the microphysical precipitation data from GPM DPR and the meteorological data from ERA5 data, we designed a more accurate algorithm for convective overshooting determination and examine the particle size, concentration, phase state and other parameters of the convective overshooting over East China. The main conclusions are:

Firstly, the horizontal distribution characteristics of convective overshooting over East China are analysed by designing a more accurate algorithm for convective overshooting determination. Statistical results indicate that the frequency of the convective overshooting over East China is very low, with a magnitude of only $10^{-3}$, with large regional differences. Convective overshooting events occur more frequently over NC and northern MEC, than SC and southern MEC, mainly because of the lower tropopause height of the former and the different underlying surfaces. The mean convective overshooting storm top height mostly ranges from 10 km to 21 km and has obvious regional distribution differences, and convective overshooting storm top height over NC is 5-6 km higher than SC.

Based on the reflectivity profiles and the rain-rate profiles provided by the GPM DPR instrument, we studied the vertical structure of precipitation within convective overshooting. The CFADs analysis of the radar reflectivity shows that radar reflectivity within convective overshooting is stronger and its storm top height is higher. The CFADs analysis also shows regional differences. Radar reflectivity of convective overshooting over NC accounts for a higher proportion below the freezing level, while MEC and SC account for a higher proportion above the freezing level, which indicate that the upward motion within convective overshooting over MEC and SC are stronger and there are more ice crystal particles. Rain rate results also show that rain rate within convective overshooting is higher, 5-10 times than that of normal precipitation. Especially, sample number of strong precipitation with grade of precipitation of heavy downpour accounts for 34.0% (NC), 46.7% (MEC), and 34.8% (SC), which remind us to pay special attention to the extreme precipitation events caused by convective overshooting.

GPM center provides particle spectrum from dual-frequency radar. Based on the DSD profiles from 2ADPR, we further investigated the microphysical structures of convective overshooting. Statistical results show that convective overshooting has unique microphysical characteristics compared with normal precipitation, with obvious regional differences. The LWP and IWP within convective overshooting are abundant, with high values of PDF distributed around 1000 g/m$^3$ and 5000 g/m$^3$ respectively. Moreover, influenced by strong updrafts, precipitation particles within convective overshooting continuously collide and grow large enough to fall, therefore, the effective radius is big, below 10 km altitude, almost exceeding 2.5 mm, which is about twice than that of normal precipitation. However, the droplet concentration within convective overshooting is relatively lower. Differences of microphysical structure between three regions are also worth noting. The effective radius of droplet over NC is slightly bigger than MEC and SC, while the droplet concentration is lower, which is speculated that it’s related to the differences of aerosol content and types over three regions.

Quantitative study of the internal microphysical characteristics within convective overshooting has not been documented previously. Findings of this study may have important implications for the microphysical evolution associated with convective overshooting, and provide more accurate precipitation microphysical parameters as the input of the model simulation. This study is the continuation of the previous research (Sun et al., 2021). In the future, we will further explore the impact of aerosol on the internal microphysical characteristics within convective overshooting, and more microphysical parameters with higher spatiotemporal resolution are expected to provide more detailed features.

**Data availability.** ERA5 data are taken from https://www.ecmwf.int/en/forecasts/datasets/reanalysis-datasets/era5. GPM DPR data are archived at https://gpm.nasa.gov/data/directory.

**Acknowledgements.** This work was funded by the National Natural Science Foundation of China Project (Grant No. 42230612) and the fellowship of China Postdoctoral Science Foundation (Grant Numbers: 2022M723011).

**Author contributions.** Sun N., Lu G.P., and Fu Y.F. framed up this study. All the authors discussed the concepts. Sun N. conducted the data analyses. Sun N. drafted the manuscript and all authors edited the manuscript.

**Competing interests.** The authors declare no competing interests.

**References**

Anderson, J. G., Wilmouth, D. M., Smith, J. B. and Sayres, D. S.: UV dosage levels in summer: Increased risk of ozone loss from convectively injected water vapor, Science, 337, 835-839, https://doi.org/10.1126/science.1222978, 2012.

Avery, M. A., Davis, S. M., Rosenlof, K. H., Ye, H. and Dessler, A. E.: Large anomalies in lower stratospheric water vapour and ice during the 2015–2016 El Niño, Nature Geoscience, 10, 405-409, https://doi.org/10.1038/ngeo2961, 2017.

Alcala, C. M. and Dessler, A. E.: Observations of deep convection in the tropics using the Tropical Rainfall Measuring Mission (TRMM) precipitation radar, Journal of Geophysical Research: Atmospheres, 107, 4792, https://doi.org/10.1029/2002JD002457, 2002.

Biondi, R., Randel, W. J., Ho, S. P., Neubert, T. and Syndergaard, S.: Thermal structure of intense convective clouds derived from GPS radio occultations, Atmospheric Chemistry and Physics, 12, 5309-5318, https://doi.org/10.5194/acp-12-5309-2012, 2012.

Bedka, K., Murillo, E. M., Homeyer, C. R., Scarino, B. and Mersiovsky, H.: The above-anvil cirrus plume: An important severe weather indicator in visible and infrared satellite imagery, Weather and Forecasting, 33, 1159-1181, https://doi.org/10.1175/WAF-D-18-0040.1, 2018.

Bethan, S., Vaughan, G., and Reid, S. J.: A comparison of ozone and thermal tropopause heights and the impact of tropopause definition on quantifying the ozone content of the troposphere, Quarterly Journal of the Royal Meteorological Society, 122(532), 929-944, https://doi.org/10.1002/qj.49712253207, 1996.

Chaboureau, J. P., Cammas, J. P., Duron, J., Mascart, P. J., Sitnikov, N. M. and Voessing, H. J.: A numerical study of tropical cross-tropopause transport by convective overshoots, Atmospheric Chemistry and Physics, 7, 1731-1740, https://doi.org/10.5194/acp-7-1731-2007, 2007.

Corti, T., Luo, B. P. and De Reus, M. et al.: Unprecedented evidence for deep convection hydrating the tropical stratosphere, Geophysical Research Letters, 35, L10810, https://doi.org/10.1029/2008GL033641, 2008.

Chemel, C., Russo, M. R., Pyle, J. A., Sokhi, R. S. and Schiller, C.: Quantifying the imprint of a severe hector thunderstorm during ACTIVE/SCOUT-O3 onto the water content in the upper troposphere/lower stratosphere, Monthly weather review, 137, 2493-2514, https://doi.org/10.1175/2008MWR2666.1, 2009.

Chae, J. H., Wu, D. L., Read, W. G. and Sherwood, S. C.: The role of tropical deep convective clouds on temperature, water vapor, and dehydration in the tropical tropopause layer (TTL), Atmospheric Chemistry and Physics, 11, 3811-3821, https://doi.org/10.5194/acp-11-3811-2011, 2011.

Danielsen, E. F.: In situ evidence of rapid, vertical, irreversible transport of lower tropospheric air into the lower tropical stratosphere by convective cloud turrets and by larger‐scale upwelling in tropical cyclones, Journal of Geophysical Research: Atmospheres, 98, 8665-8681, https://doi.org/10.1029/92JD02954, 1993.

De Reus, M., Borrmann, S. and Bansemer, A. et al: Evidence for ice particles in the tropical stratosphere from in-situ measurements, Atmospheric Chemistry and Physics, 9, 6775-6792, https://doi.org/10.5194/acp-9-6775-2009, 2009.

Danielsen, E. F., Hipskind, R. S. and Gaines, S. E. et al.: Three-dimensional analysis of potential vorticity associated with tropopause folds and observed variations of ozone and carbon monoxide, Journal of Geophysical Research: Atmospheres, 92(D2), 2103-2111, https://doi.org/10.1029/JD092iD02p02103, 1987.

Fueglistaler, S., Wernli, H. and Peter, T.: Tropical troposphere - to - stratosphere transport inferred from trajectory calculations, Journal of Geophysical Research: Atmospheres, 109, D03108, https://doi.org/10.1029/2003JD004069, 2004.

Frey, W., Schofield, R. and Hoor, P. et al.: The impact of overshooting deep convection on local transport and mixing in the tropical upper troposphere/lower stratosphere (UTLS), Atmospheric Chemistry and Physics, 15, 6467-6486, https://doi.org/10.5194/acp-15-6467-2015, 2015.

General Administration of Quality Supervision, Inspection and Quarantine of the People's Republic of China: Standardization Administration of the People's Republic of China, GB/T 28592—2012 Grade of precipitation, Standards Press of China, 2012.

Grosvenor, D. P., Choularton, T. W., Coe, H. and Held, G.: A study of the effect of overshooting deep convection on the water content of the TTL and lower stratosphere from Cloud Resolving Model simulations, Atmospheric Chemistry and Physics, 7, 4977-5002, https://doi.org/10.5194/acp-7-4977-2007, 2007.

Gettelman, A., Salby, M. L. and Sassi, F.: Distribution and influence of convection in the tropical tropopause region, Journal of Geophysical Research: Atmospheres, 107, 4080, https://doi.org/10.1029/2001JD001048, 2002.

Homeyer, C. R. and Kumjian, M. R.: Microphysical characteristics of overshooting convection from polarimetric radar observations, Journal of the Atmospheric Sciences, 72, 870-891, https://doi.org/10.1175/JAS-D-13-0388.1, 2015.

Hoffmann, L., Günther, G. and Li, D. et al.: From ERA-Interim to ERA5: the considerable impact of ECMWF's next-generation reanalysis on Lagrangian transport simulations, Atmospheric Chemistry and Physics, 19, 3097-3124, https://doi.org/10.5194/acp-19-3097-2019, 2019.

Highwood, E. J. and Hoskins, B. J.: The tropical tropopause, Quarterly Journal of the Royal Meteorological Society, 124, 1579-1604, https://doi.org/10.1002/qj.49712454911, 1998.

Holton, J. R., Haynes, P. H. and McIntyre, M. E. et al.: Stratosphere-troposphere exchange. Reviews of geophysics, 33(4), 403-439, https://doi.org/10.1029/95RG02097, 1995.

Jensen, E. J., Ackerman, A. S. and Smith, J. A.: Can overshooting convection dehydrate the tropical tropopause layer?, Journal of Geophysical Research: Atmospheres, 112, D11209, https://doi.org/10.1029/2006JD007943, 2007.

Johnston, B. R., Xie, F. and Liu, C.: The effects of deep convection on regional temperature structure in the tropical upper troposphere and lower stratosphere, Journal of Geophysical Research: Atmospheres, 123, 1585-1603, https://doi.org/10.1002/2017JD027120, 2018.

Khaykin, S., Pommereau, J. P. and Korshunov, L. et al.: Hydration of the lower stratosphere by ice crystal geysers over land convective systems, Atmospheric Chemistry and Physics, 9, 2275-2287, https://doi.org/10.5194/acp-9-2275-2009, 2009.

Langmuir, I.: The production of rain by a chain reaction in cumulus clouds at temperatures above freezing, Journal of the Atmospheric Sciences, 5(5), 175-192, https://doi.org/10.1175/1520-0469(1948)005<0175:TPORBA>2.0.CO;2, 1948.

Liu, N. and Liu, C.: Global distribution of deep convection reaching tropopause in 1 year GPM observations, Journal of Geophysical Research: Atmospheres, 121, 3824-3842, https://doi.org/10.1002/2015JD024430, 2016.

Liu, N., Liu, C. and Hayden, L.: Climatology and detection of overshooting convection from 4 years of GPM precipitation radar and passive microwave observations, Journal of Geophysical Research: Atmospheres, 125, e2019JD032003, https://doi.org/10.1029/2019JD032003, 2020.

Liu, C. and Zipser, E. J.: Global distribution of convection penetrating the tropical tropopause, Journal of Geophysical Research: Atmospheres, 110, D23104, https://doi.org/10.1029/2005JD006063, 2005.

Liu, P., Wang, Y., Feng, S., Li, C. Y. and Fu, Y. F.: Climatological characteristics of overshooting convective precipitation in summer and winter over the tropical and subtropical regions, Chin. J. Atmos. Sci., 36, 579-589, https://doi.org/10.3878/j.issn.1006-9895.2011.11109, 2012.

Line, W. E., Schmit, T. J., Lindsey, D. T. and Goodman, S. J.: Use of geostationary super rapid scan satellite imagery by the Storm Prediction Center, Weather and Forecasting, 31, 483-494, https://doi.org/10.1175/WAF-D-15-0135.1, 2016.

Machado, L. A. T., Rossow, W. B., Guedes, R. L. and Walker, A. W.: Life cycle variations of mesoscale convective systems over the Americas, Monthly Weather Review, 126, 1630-1654, https://doi.org/10.1175/1520-0493(1998)126<1630:LCVOMC>2.0.CO;2, 1998.

Muhsin, M., Sunilkumar, S. V., Ratnam, M. V., Parameswaran, K., Murthy, B. K. and Emmanuel, M.: Effect of convection on the thermal structure of the troposphere and lower stratosphere including the tropical tropopause layer in the South Asian monsoon region, Journal of Atmospheric and Solar-Terrestrial Physics, 169, 52-65, https://doi.org/10.1016/j.jastp.2018.01.016, 2018.

Marion, G. R., Trapp, R. J. and Nesbitt, S. W.: Using overshooting top area to discriminate potential for large, intense tornadoes, Geophysical Research Letters, 46, 12520-12526, https://doi.org/10.1029/2019GL084099, 2019.

Rodriguez‐Franco, J. J. and Cuevas, E.: Characteristics of the subtropical tropopause region based on long‐term highly resolved sonde records over Tenerife, Journal of Geophysical Research: Atmospheres, 118, 10-754, https://doi.org/10.1002/jgrd.50839, 2013.

Rossow, W. B. and Pearl, C.: 22‐year survey of tropical convection penetrating into the lower stratosphere, Geophysical research letters, 34, L04803, https://doi.org/10.1029/2006GL028635, 2007.

Solomon, S., Rosenlof, K. H. and Portmann, R. W. et al.: Contributions of stratospheric water vapor to decadal changes in the rate of global warming, Science, 327, 1219-1223, https://doi.org/10.1126/science.1182488, 2010.

Sherwood, S. C. and Dessler, A. E.: A model for transport across the tropical tropopause, Journal of the Atmospheric Sciences, 58, 765-779, https://doi.org/10.1175/1520-0469(2001)058<0765:AMFTAT>2.0.CO;2, 2001.

Smith, J. B., Wilmouth, D. M., and Bedka, K. M. et al.: A case study of convectively sourced water vapor observed in the overworld stratosphere over the United States, Journal of Geophysical Research: Atmospheres, 122(17), 9529-9554, https://doi.org/10.1002/2017JD026831, 2017.

Sun, N., Fu, Y., Zhong, L., Zhao, C. and Li, R.: The Impact of Convective Overshooting on the Thermal Structure over the Tibetan Plateau in Summer Based on TRMM, COSMIC, Radiosonde, and Reanalysis Data, Journal of Climate, 34, 8047-8063, https://doi.org/10.1175/JCLI-D-20-0849.1, 2021.

Sun, N., Fu, Y., Zhong, L. and Li, R.: Aerosol effects on the vertical structure of precipitation in East China, npj Climate and Atmospheric Science, 5, 60, https://doi.org/10.1038/s41612-022-00284-0, 2022a.

Sun, N., Zhong, L., Zhao, C., Ma, M. and Fu, Y.: Temperature, water vapor and tropopause characteristics over the Tibetan Plateau in summer based on the COSMIC, ERA-5 and IGRA datasets, Atmospheric Research, 266, 105955, https://doi.org/10.1016/j.atmosres.2021.105955, 2022b.

Sherwood, S. C., Horinouchi, T. and Zeleznik, H. A.: Convective impact on temperatures observed near the tropical tropopause, Journal of Atmospheric Sciences, 60, 1847-1856, https://doi.org/10.1175/1520-0469(2003)060<1847:CIOTON>2.0.CO;2, 2003.

Takahashi, H. and Luo, Z. J.: Characterizing tropical overshooting deep convection from joint analysis of CloudSat and geostationary satellite observations, Journal of Geophysical Research: Atmospheres, 119, 112-121, https://doi.org/10.1002/2013JD020972, 2014.

Wang, X., Huang, Y., and Qu, Z. et al.: Convectively Transported Water Vapor Plumes in the Midlatitude Lower Stratosphere, Journal of Geophysical Research: Atmospheres, 128(4), e2022JD037699, https://doi.org/10.1029/2022JD037699, 2023.

Werner, F., Schwartz, M. J., and Livesey, N. J. et al.: Extreme outliers in lower stratospheric water vapor over North America observed by MLS: Relation to overshooting convection diagnosed from colocated Aqua‐MODIS data, Geophysical Research Letters, 47(24), e2020GL090131, https://doi.org/10.1029/2020GL090131, 2020.

World Meteorological Organization.: Meteorology—A three‐dimensional science: Second session of the commission for aerology, WMO Bull, 4, 134-138, 1957.

Xia, J.: Research on climatic regionalization of China and characteristics of temperature, humidity and wind in precipitation cloud, University of Science and Technology of China, 2015.

Xu, W.: Thunderstorm climatologies and their relationships to total and extreme precipitation in China, Journal of Geophysical Research: Atmospheres: 125, e2020JD033152, https://doi.org/10.1029/2020JD033152, 2020.

Yuter, S. E. and Houze, R. A.: Three-dimensional kinematic and microphysical evolution of Florida cumulonimbus. Part II: Frequency distributions of vertical velocity, reflectivity, and differential reflectivity, Monthly Weather Review, 123(7), 1941-1963, https://doi.org/10.1175/1520-0493(1995)123<1941:TDKAME>2.0.CO;2, 1995.

Zhang, A. and Fu, Y.: Life cycle effects on the vertical structure of precipitation in East China measured by Himawari-8 and GPM DPR, Monthly Weather Review, 146, 2183-2199, https://doi.org/10.1175/MWR-D-18-0085.1, 2018.

Zahn, A., Brenninkmeijer, C. A. M., and Van Velthoven, P. F. J.: Passenger aircraft project CARIBIC 1997–2002, Part I: the extratropical chemical tropopause, Atmospheric Chemistry and Physics Discussions, 4(1), 1091-1117, https://doi.org/10.5194/acpd-4-1091-2004, 2004.

**Tables**

**Table1.** The sample number of total precipitation, convective precipitation, and convective overshooting over NC, MEC, and SC.

| Sample number (count, ct) | NC | MEC | SC |
|---|---|---|---|
| Total Precipitation | 652489 | 546313 | 319127 |
| Convective Precipitation | 111903 | 137674 | 111900 |
| Convective Overshooting | 2394 | 582 | 296 |

**Figures**

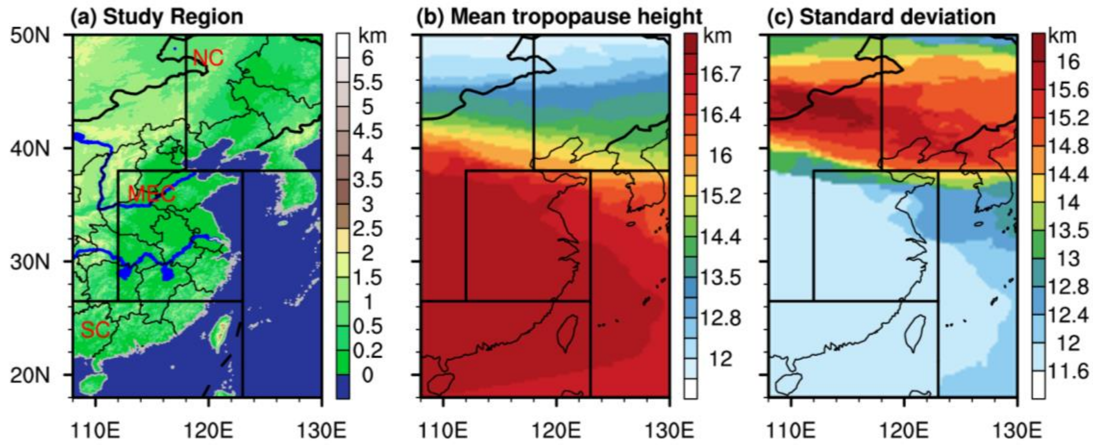


**Figure 1.** Study areas and their tropopause characteristics. **(a)** Regionalization of East China (Black boxes: Divisions between NC, MEC and SC, and only the land surface is studied) and their terrain features**. (b)** Climatological mean of tropopause height from 2014 to 2020 in summer (June, July and August). **(c)** Distribution of standard deviation of tropopause height.

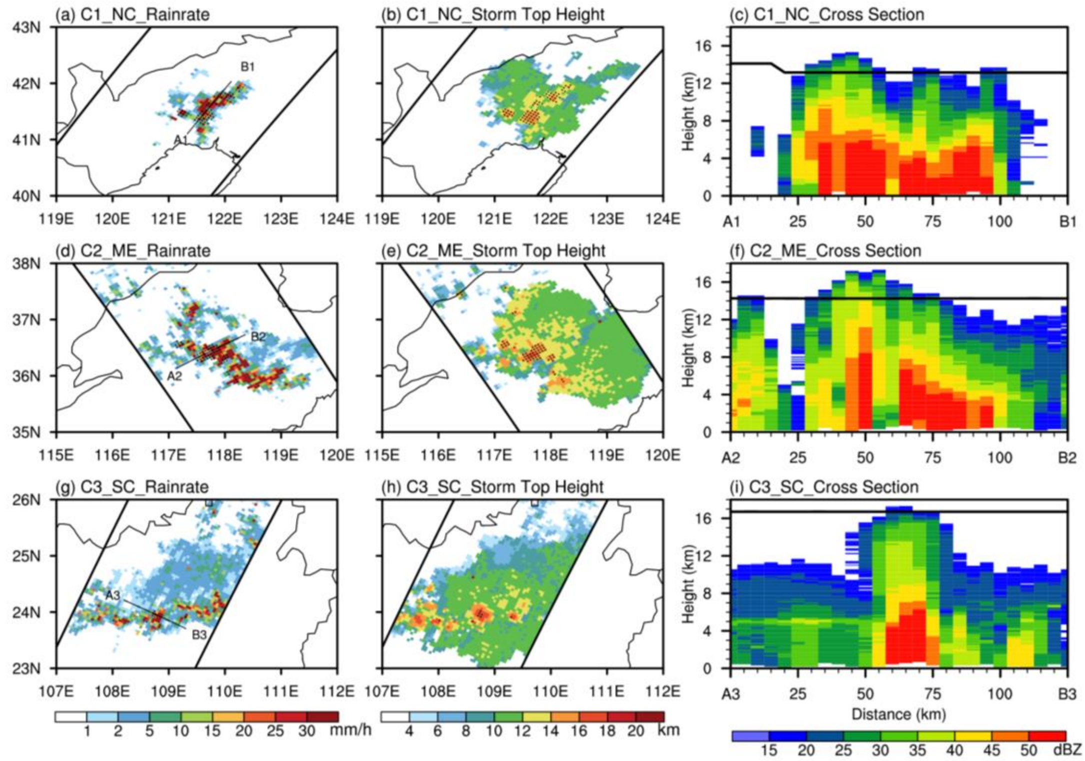


**Figure 2.** Precipitation characteristics of convective overshooting cases. **(a)** Distribution of rain rate of Case 1 (C1). (The pixels in which convective overshooting occurs are marked as black points). **(b)** Distribution of storm top height of C1. **(c)** Radar reflectivity cross section along A1B1 and the black line show the tropopause height along A1B1. **(d)** Distribution of rain rate of C2. **(e)** Distribution of storm top height of C2. **(f)** Radar reflectivity cross section along A2B2. **(g)** Distribution of rain rate of C3. **(h)** Distribution of storm top height of C3. **(i)** Radar reflectivity cross section along A3B3.

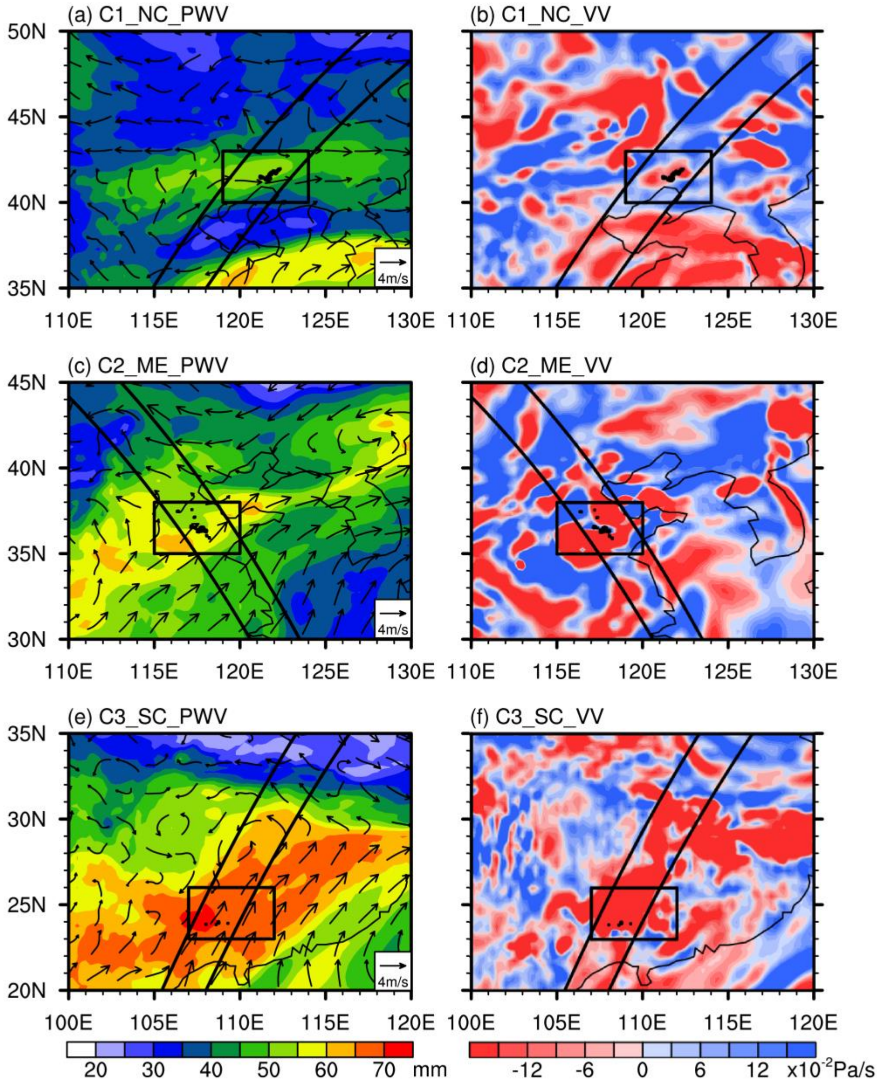


**Figure 3.** Characteristics of large scale circulation of convective overshooting cases. **(a)** Distribution of precipitable water vapor (PWV) and streamlines at 850 hPa of C1. The area where the case occurred is marked as big black boxes and the pixels in which convective overshooting occurs are marked as little black boxes. The black line is the GPM detection orbit. **(b)** Distribution of vertical velocity (VV) at 500 hPa of C1. **(c)** Distribution of PWV and streamlines of C2. **(d)** Distribution of VV of C2. **(e)** Distribution of PWV and streamlines of C3. **(f)** Distribution of VV of C3.

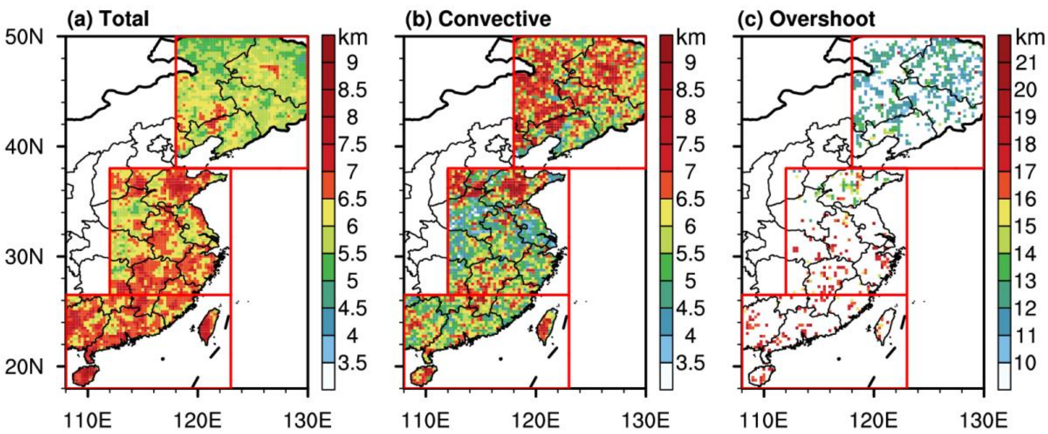


**Figure 4.** Geographical distribution of storm top height. **(a)** Distribution of storm top height for total precipitation. **(b)** Distribution of storm top height for convective precipitation. **(c)** Distribution of storm top height for convective overshooting.

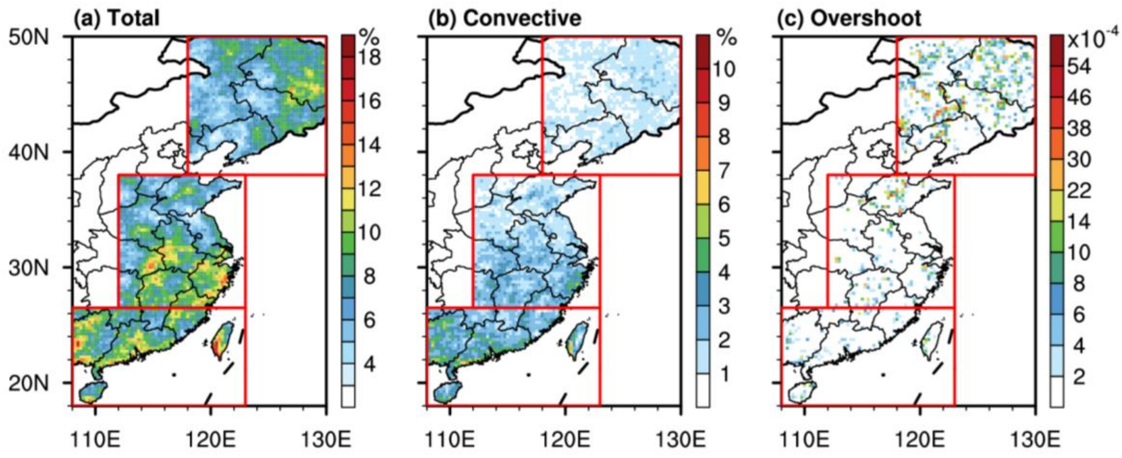


**Figure 5.** Precipitation frequency. **(a)** Frequency of total precipitation. **(b)** Frequency of convective precipitation. **(c)** Frequency of convective overshooting.

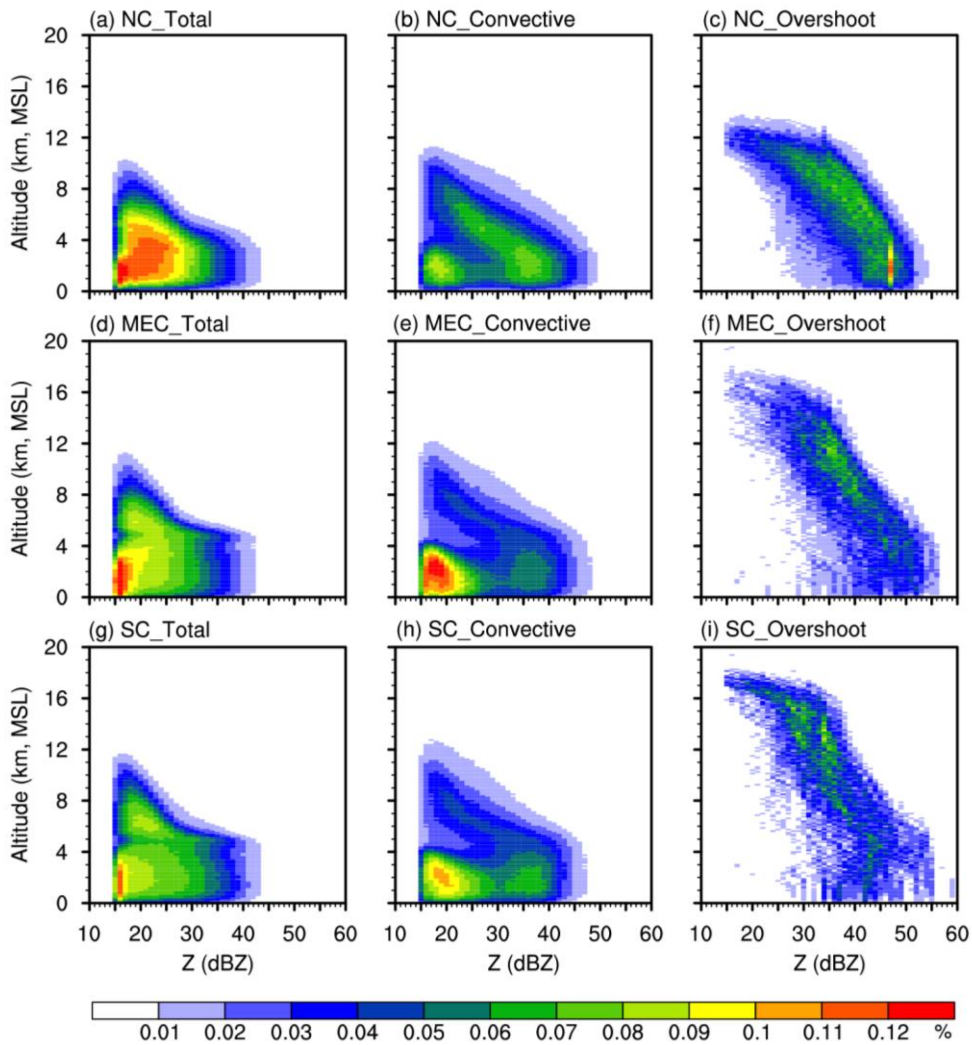


**Figure 6.** Contoured Frequency by Altitude Diagrams (CFADs) of radar reflectivity. **(a)** CFADs for total precipitation over NC. **(b)** CFADs for convective precipitation over NC. **(c)** CFADs for convective overshooting over NC. **(d)** CFADs for total precipitation over MEC. **(e)** CFADs for convective precipitation over MEC. **(f)** CFADs for convective overshooting over MEC. **(g)** CFADs for total precipitation over SC. **(h)** CFADs for convective precipitation over SC. **(i)** CFADs for convective overshooting over SC.

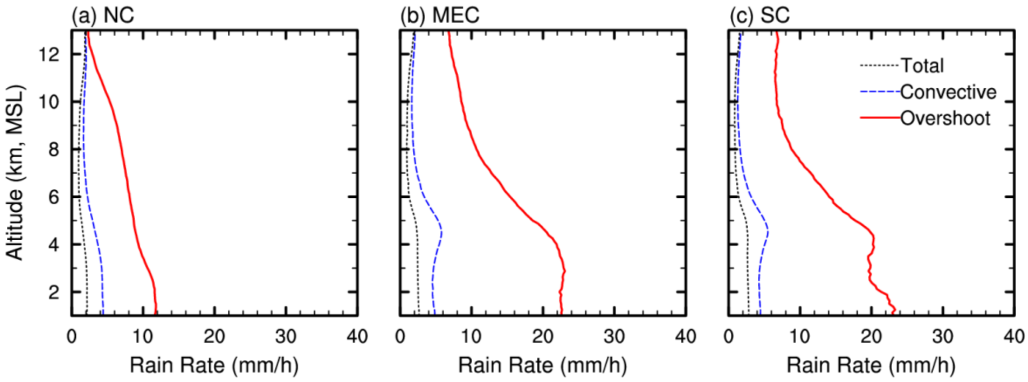


**Figure 7.** Rain rate profiles for total precipitation, convective precipitation and convective overshooting (Red lines are convective overshooting; Blue lines are the convective precipitation; Black lines are the total precipitation). **(a)** The rain rate profiles over NC. **(b)** The rain rate profiles over MEC. **(c)** The rain rate profiles over SC.

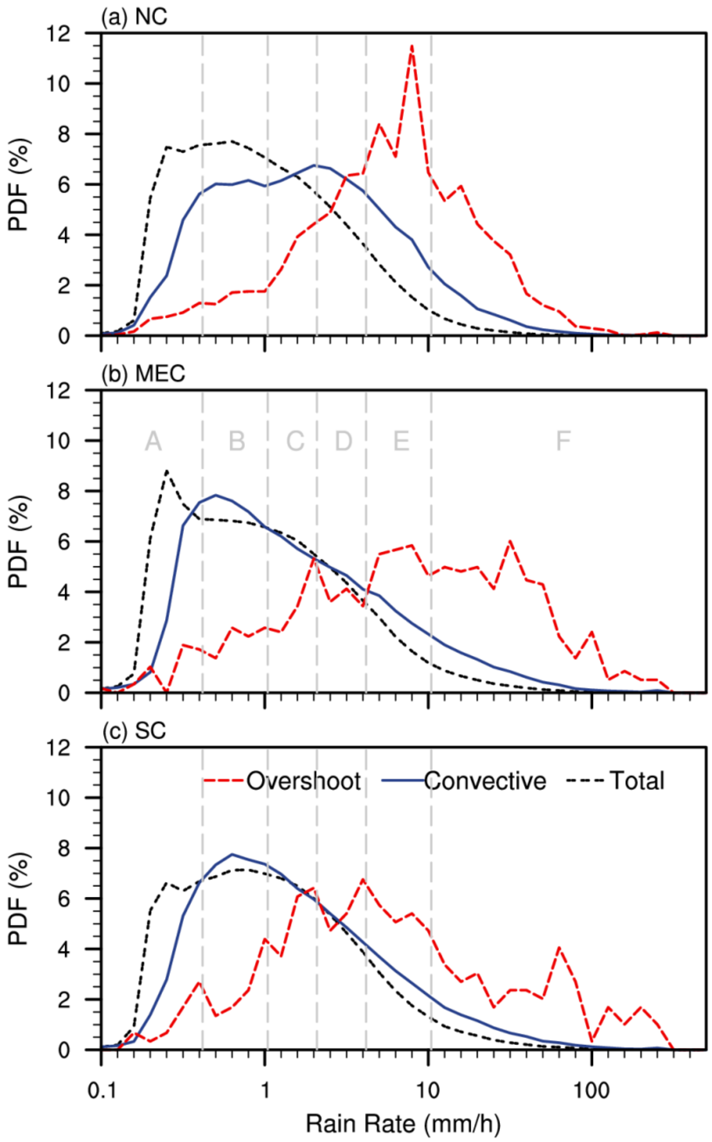


**Figure 8.** Probability Density Function (PDF) of Near Surface Rain Rate (NSRR). **(a)** PDF of NSRR in NC. **(b)** PDF of NSRR in MEC. **(c)** PDF of NSRR in SC.

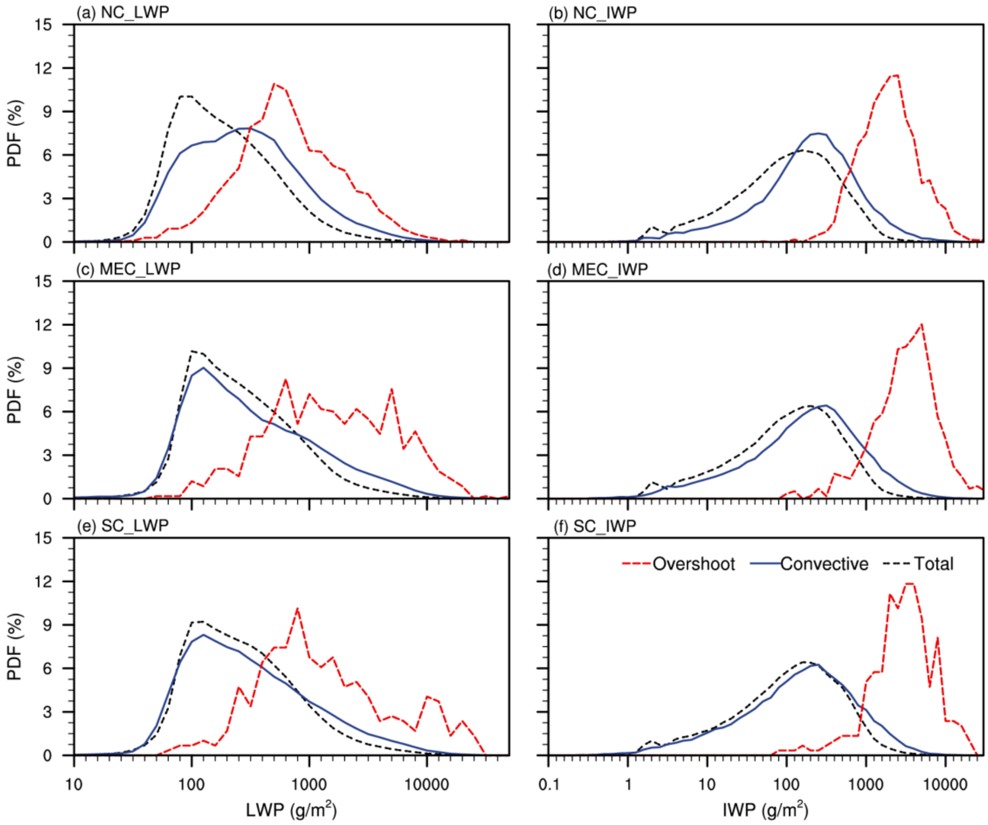


**Figure 9.** PDF of Liquid Water Path (LWP) and Ice Water Path (IWP). **(a)** PDF of LWP over NC. **(b)** PDF of IWP over NC. **(c)** PDF of LWP over MEC. **(d)** PDF of IWP over MEC. **(e)** PDF of LWP over SC. **(f)** PDF of IWP over SC.

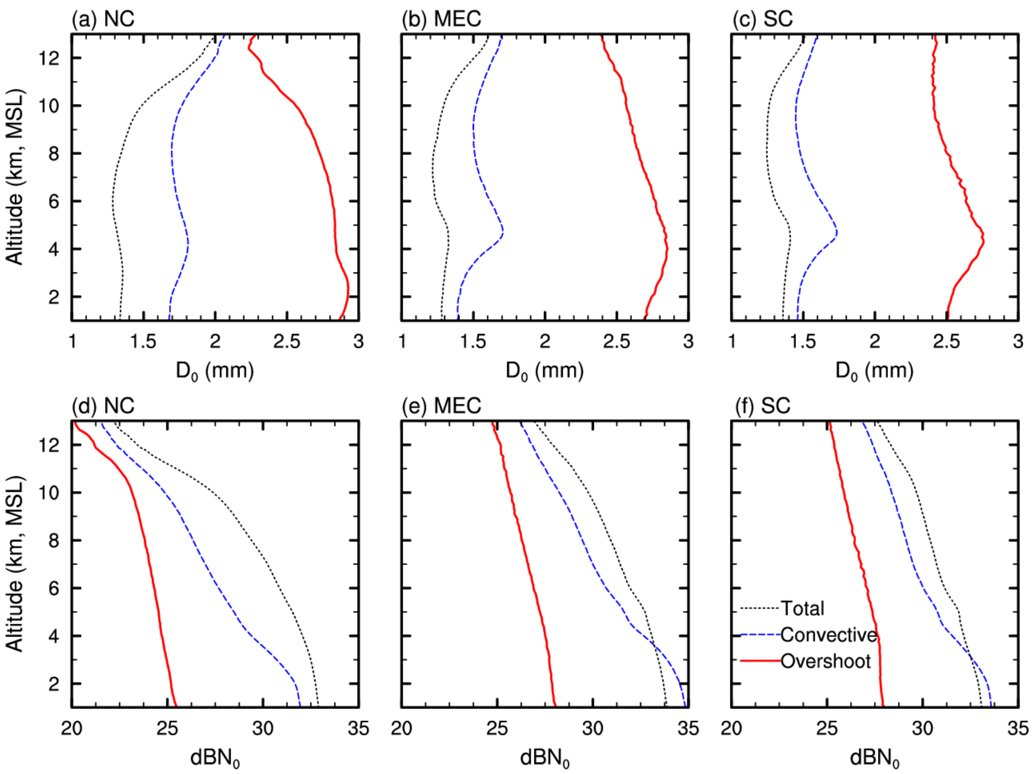


**Figure 10.** The droplet concentration ($dBN_0$) and effective radius ($D_0$) profiles for total precipitation, convective precipitation and convective overshooting over NC, MEC and SC. **(a)** The $dBN_0$ profiles over NC. **(b)** The $dBN_0$ profiles over MEC. **(c)** The $dBN_0$ profiles over SC. **(d)** $D_0$ profiles over NC. **(e)** $D_0$ profiles over MEC. **(f)** $D_0$ profiles over SC.